JATIS Journal of Astronomical Telescopes, Instruments, and Systems

RESEARCH PAPER

X-ray spectral performance of the Sony IMX290 CMOS sensor near Fano limit after a per-pixel gain calibration

Benjamin Schneider,[a,*] Gregory Prigozhin,[a] Richard F. Foster,[a] Marshall W. Bautz,[a] Hope Fu,[a] Catherine E. Grant,[a] Sarah Heine,[a] Jill Juneau,[a] Beverly LaMarr,[a] Olivier Limousin,[b] Nathan Lourie,[a] Andrew Malonis,[a] and Eric D. Miller[a]

[a]Massachusetts Institute of Technology, Kavli Institute for Astrophysics and Space Research, Cambridge, Massachusetts, United States

[b]Université Paris-Saclay, Université Paris Cité, CEA, CNRS, AIM, Gif-sur-Yvette, France

ABSTRACT. The advent of back-illuminated complementary metal–oxide–semiconductor (CMOS) sensors and their well-known advantages over charge-coupled devices make them an attractive technology for future X-ray missions. However, numerous challenges remain, including improving their depletion depth and identifying effective methods to calculate per-pixel gain conversion. We have tested a commercial Sony IMX290LLR CMOS sensor under X-ray light using an ^{55}Fe radioactive source and collected X-ray photons for ∼15 consecutive days under stable conditions at regulated temperatures of 21°C and 26°C. At each temperature, the data set contained enough X-ray photons to produce one spectrum per pixel consisting only of single-pixel events. We determined the gain dispersion of its 2.1 million pixels using the peak fitting and the energy calibration via correlation (ECC) methods. We measured a gain dispersion of 0.4% at both temperatures and demonstrated the advantage of the ECC method in the case of spectra with low statistics. The energy resolution at 5.9 keV after the per-pixel gain correction is improved by $\gtrsim$10 eV for single-pixel and all event spectra, with single-pixel event energy resolution reaching 123.6 ± 0.2 eV, close to the Fano limit of silicon sensors at room temperature. Finally, our long data acquisition demonstrated the excellent stability of the detector over more than 30 days under a flux of 10^4 photons per second.

 [DOI: 10.1117/1.JATIS.10.3.038001]

Keywords: X-ray detectors; complementary metal–oxide–semiconductor sensors; energy calibration; X-ray spectral performance

Paper 24095G received Jul. 3, 2024; revised Sep. 3, 2024; accepted Sep. 5, 2024; published Sep. 28, 2024.

1 Introduction

For X-ray astronomy, charge-coupled devices (CCDs) have been successfully used over the past decades[1–5] and are still proposed for upcoming and future X-ray missions.[6–9] CCDs are a mature technology that has benefited from continuous development, achieving very low noise and excellent uniformity. The next generation of X-ray missions requires higher readout speed, lower power consumption, and better radiation tolerance while maintaining high-quality imaging and spectral performance. Recent improvements in complementary metal–oxide–semiconductor (CMOS) detectors and the use of back-side illuminated CMOS offer a promising alternative

*Address all correspondence to Benjamin Schneider, bschn@mit.edu

to CCDs for future X-ray instruments. In particular, CMOS detectors provide a high readout frame rate per second (fps), low readout noise, and low power consumption and can be operated at room temperature. In addition, the active pixel design of CMOS prevents the inherent and growing charge transfer inefficiency affecting CCD performance over time due to space radiation. Their relatively low cost compared with CCDs makes them an attractive technology for wide-field X-ray instruments. The wide-field X-ray telescope, on board the Einstein Probe[10] mission, launched in early 2024, and its pathfinder the Lobster Eye Imager for Astronomy flight experiment,[11] launched in 2022, are the first X-ray missions to use scientific CMOS sensors in space environment and have already demonstrated promising results.[12,13] However, many challenges remain before CMOS sensors can be considered a viable alternative for more X-ray applications. CMOS devices suffer from lower depletion depths and reduced X-ray quantum efficiency compared with CCDs,[14] although manufacturers have been improving X-ray optimized designs.[15,16] The highly parallelized readout architecture of CMOS devices, which provides their high readout rate, also leads to higher variation in gain from pixel-to-pixel compared with that from the single readout node of a CCD array. This gain variation can degrade the spectral energy resolution.[15–19] Improved procedures to characterize the pixel-to-pixel gain variation inherent to CMOS devices can significantly improve their spectral energy resolution. One commercial CMOS sensor that has shown promise for the detection of X-rays is the Sony IMX290LLR (1920×1080 2.9 μm pixels), which is optimized for optical light and routinely used for astrophotography or security camera systems. However, its low-noise ($\sim 2\,e-$ rms) and back-side illuminated design makes it suitable for detecting X-rays. Previous works have successfully tested the device under X-ray light and demonstrated its excellent spectral performance from 250 eV to 6.4 keV.[20,21] In this paper, we investigate an efficient technique to characterize per-pixel conversion gain calibration using a CMOS sensor. We measure and correct the per-pixel gains of the 2.1 million pixels composing the Sony IMX290 CMOS sensor. We then derive the 5.9 keV spectral performance of the device after correcting for gain dispersion. We finally report on the stability of the system over time, based on the long acquisition periods required to measure the gain of each pixel.

2 Experimental Setup

Our setup employs the Imaging Development Systems (IDS) UI-3862LE-M camera offering a board-level, low-cost, compact, and versatile system. The board is equipped with a Sony STARVIS I IMX290 CMOS sensor (see Table 1), which is a low-noise monochrome back-side

Table 1 Main characteristics of the IDS UI-3862LE camera equipped with the Sony IMX290 CMOS sensor.

Camera model	UI-3862LE-M
Sensor model	IMX290LLR-C
Imaging area	5.610×3.175 mm
Number of pixels	1936×1096
Pixel size	2.9 μm
Pixel clock range	20 to 474 MHz
Frame rate	Up to 120 fps
Exposure time	0.011 ms to 120 s
Readout noise	1.9 $e-$ rms
ADC	12 bit
Shutter	Rolling shutter
Camera power	0.9 to 1.5 W

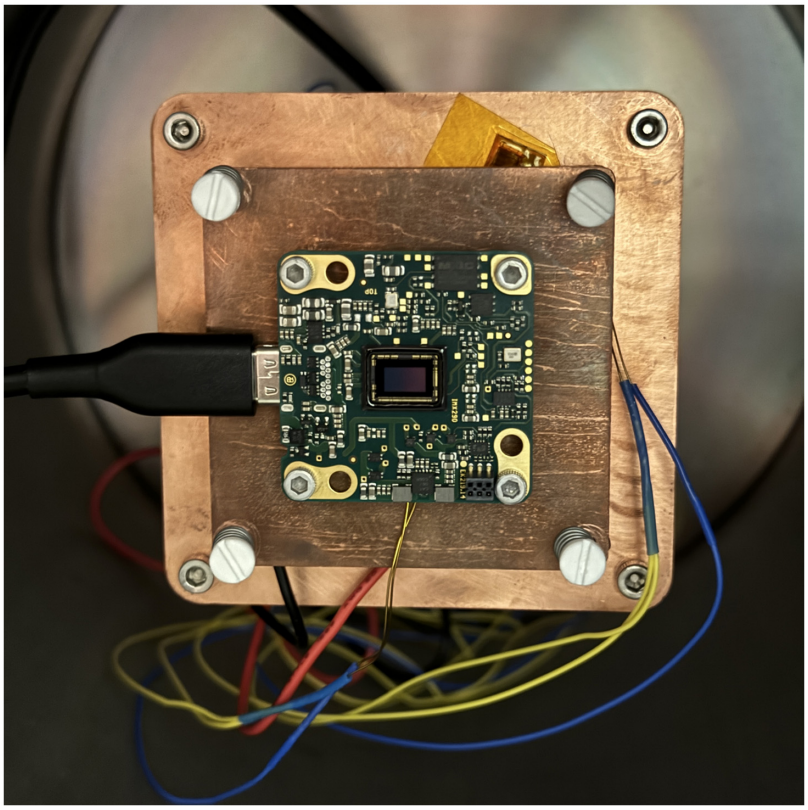

Fig. 1 Picture of the experimental setup. The CMOS sensor is visible at the center of the image and surrounded by its readout electronics. The camera is connected to the cold side of the TEC (not visible) via a copper plate. The hot and cold sides are held together with Polytetrafluoroethylene (PTFE) plastic screws to minimize the heating load.

illuminated device making it suitable to detect X-ray light. The board uses USB3.1 for command/control, power, and image transfer enabling a readout speed of up to 120 fps. As is standard for X-ray imaging, the cover glass over the top of the sensor package was removed to ensure the detection of X-ray photons below 10 keV. The camera was installed in a cryostat and operated under vacuum. A thermoelectric cooler (TEC) was used to cool down the camera and a proportional–integral–derivative (PID) controller was implemented to maintain a constant temperature (± 0.2°C) during measurements. The hot and cold sides of the TEC were clamped to copper interfaces to maximize thermal conduction and were monitored by two resistance temperature detectors. The hot side was connected to a power feedthrough to evacuate the heat produced by the camera and TEC in the cryostat. External to the power feedthrough, a cold plate was attached and liquid-cooled by a chiller at 10°C, which maintained the hot side at a constant temperature and improved the TEC cooling capacity (see Fig. 1).

Preliminary tests illuminated the sensor with a radioactive source of ^{55}Fe producing Mn-Kα (5.90 keV) and Mn-Kβ (6.49 keV) emission lines. During that phase, the analog gain of the image sensor was tuned to obtain a conversion gain of 1 $e-$/analog-to-digital unit (ADU) and maintain the electronic noise as low as possible. We also illuminated the system with a source composed of ^{210}Po and Teflon to produce fluorescence lines of C-K (0.53 keV) and F-K (0.68 keV). Both sources validate the ability of this sensor to detect soft X-ray photons down to 277 eV, as previously observed in 20. Only the results from the ^{55}Fe measurements are presented in this paper.

3 Real-Time Data Processing

We used the uEye interface for Python (PyuEye), provided by IDS, to set the camera settings (e.g., fps, pixel clocks, gain) and access full raw frames. The hot pixel correction offered by the Application Programming Interface was disabled to prevent single X-ray events from being

considered hot pixels. The camera was operated at 10 fps, with each frame producing 4.2 MB of data, thus generating ∼2.5 GB every minute. For experimental testing, the large amount of data generated raised multiple challenges, especially in terms of storage capacity and post-processing time. In addition, pixels hit by X-ray photons represent only a small fraction of the entire image. To overcome these challenges, we developed an algorithm to process the frames in real time to only extract and save valid X-ray events, which drastically reduced memory usage by only keeping the relevant information deposited by X-ray photons in each frame.

For real-time X-ray event finding, the imaging sequence starts by taking a series of initial frames, of at least 200 frames, to compute the offset map. The map is then regularly updated to mitigate, for instance, the emergence of new flickering hot pixels over time. When a new frame is transferred, the offset map is subtracted in real time, and the resulting pixel amplitudes are compared with an event threshold where all pixels above it are considered valid X-ray events. The event threshold can be defined as a fixed value or pixel-dependent using the initial frames of the sequence. In practice, we use a fixed event threshold value for all pixels tuned based on the best resulting spectral performance observed. The island around each valid event is extracted and finally saved. Given the small pixel size of the sensor (2.9 μm) and the likely small thickness of the device (<10 μm), we consider islands from 3×3 up to 7×7 pixels to ensure that the extraction of X-ray events extends over multiple pixels. Then, a list of events considered valid X-ray photons is regularly saved. Possible remaining hot pixels are rejected during the offline post-processing based on their anomalous count rate. Although the frames can be partially reconstructed at a later time, one of the main limitations of this approach is that event extraction cannot be run again with other parameters such as different event threshold values or larger event island sizes. The algorithm was successfully run on a Raspberry Pi 4B and an Intel Core i7-13700K processor. The number of frames per second that can be processed by the CPU depends on many factors, such as the counting regime or the event island size. For our study, running at 10 frames per second allowed us to extract ∼7000 events per second.

4 Energy Calibration

4.1 Calibration Methods

In CMOS architecture, charge-voltage conversion and the first amplification stage are implemented directly at the pixel level. This means that each pixel has its own amplification circuit, likely generating non-uniform conversion gain between pixels. In addition to the Fano and electronic noise, small variations in the pixel gains can broaden the energy line and degrade the energy resolution of the sensor. To overcome this degradation, correction of the pixel-to-pixel gain dispersion can potentially improve the spectral performance. The X-ray calibration process involves illuminating the detector with a source emitting X-ray photons at known energies, ideally with several lines to increase calibration accuracy. The correlation between the observed spectrum (in ADU) and the known spectrum (in keV) can be measured using different approaches. A common method is the so-called "peak fitting." It consists of fitting every line in the observed ADU spectrum with a Gaussian function to determine the line centroid and find the relation between these centers and the expected incident photon energy. A linear relation usually provides a reliable energy calibration, but a more complex relation (e.g., quadratic) can be employed to correct for non-linear readout electronic effects over a large energy range. Another possible approach is the "energy calibration via correlation" (ECC)[22,23] initially employed for CdTe semiconductor detectors. The method relies on finding the maximum correlation between a synthetic spectrum (template) of the incident source and the observed spectrum. Similar to the peak fitting approach, the ECC method can be used to find linear or more complex relations. ECC offers multiple possible advantages over peak fitting. It allows a more robust and accurate calibration using lines and background as a whole, provides flexible ways of tracking the energy calibration evolution over time using a previously calibrated dataset, and has been shown to outperform peak fitting in the case of a low-statistics spectrum.[22] The latter is particularly interesting for energy calibration of CMOS sensors, where a large number of pixel gains need to be calculated, causing significant challenges in generating sufficient statistics for each pixel. Both methods were used in our study, and their results have been compared to determine the strength of each approach (Sec. 4.4).

4.2 Data Collection for the Energy Calibration

The Sony IMX290 CMOS sensor is composed of 2.1 million pixels, and its precise energy calibration requires the measurement of a gain for each pixel. This requires generating a spectrum for each pixel, where each pixel spectrum is composed of single-pixel events to avoid mixing the gains of adjacent pixels. It also means collecting data under stable conditions to limit the contribution of external effects (e.g., temperature) on the gains measured.

To keep the acquisition time at a reasonable level, we illuminated the sensor with a bright ^{55}Fe radioactive source (∼38 MBq), which produces ∼7000 events/s on the detector. The camera was run at 10 fps to limit the pile-up and reduce the dark current to a negligible level for the operating conditions. To limit the data flow and save storage space, we performed real-time event extraction to capture only the relevant information, as described in Sec. 3. The camera temperature was kept within 0.2°C throughout the acquisition using a TEC and a PID loop.

The ^{55}Fe radioactive source produces two main energy lines at 5.90 and 6.49 keV. The fraction of single-pixel events obtained at 5.9 keV was measured to be ∼30%. Previous work on the IMX290 attempted to measure the gain dispersion by dividing the sensor area into 5×5 sub-areas and measured a dispersion of 0.14%.[20] Although this method can give a rough idea of the gain dispersion, it can still mix in small-scale gain variations caused by mismatch variations of the pixel elements (e.g., transistors, photodiodes) during the manufacturing processes.

We performed ^{55}Fe simulations to determine the optimal number of single-pixel events per pixel to accurately recover a given gain dispersion. We estimated that for a gain dispersion of ∼0.1%, more than 1000 events per pixel are needed with both calibration methods. A more precise estimate of the optimal number of individual events is discussed further in Sec. 6. Based on these estimates and the count rate produced by the radioactive source, we targeted 14 consecutive days of acquisition to achieve ∼1200 events per pixel.

Our acquisition sequence consists of two main steps. First, the offset map is calculated using 300 frames (30 s of data collection). The setup configuration prevents the removal of the radioactive source during this acquisition time. We thus derived the offset map by applying a sigma clipping to mitigate the effect of X-ray events on the calculation. The second phase consists of collecting 6000 consecutive frames (10 min of acquisition) and performing a real-time X-ray event extraction using the offset map, as described in Sec. 3. We repeat this sequence every 10 min for 14 days to track the evolution of the offsets and to ensure efficient real-time event extraction. When the camera is turned on, the temperature may temporarily fluctuate faster due to the additional heat produced by the readout electronics until a new equilibrium is reached. To have only datasets with a stable camera temperature, the first 1.5 h of datasets was removed from our post-processing analysis.

4.3 Post-processing and Per-Pixel Spectrum

The data set collected over 14 days generated 1 TB of data. Processing such a large volume of data remains challenging with current laboratory computing resources. Thus, we performed the post-processing analysis on the Massachusetts Institute of Technology (MIT) SuperCloud,[24] a supercomputing cluster at MIT that currently provides individual allocation of 384 CPUs. The post-processing analysis was designed and optimized to minimize computational time, resulting in ∼1 day of computation on 384 CPUs. Single-pixel events were first extracted from each 10-min event list file and then redistributed to their respective pixels along the 14 days of acquisition. Figure 2(a) shows the count map of the 2.1 million pixels from the measurement. We determined a median count of 1368 and observed a non-uniform distribution of counts across the sensor area. The lower left corner had a count of more than 2000, whereas the upper right corner had a count of ∼500. This could be due to a misalignment of the ^{55}Fe source with the sensor creating an inhomogeneous illumination pattern. The potential impact of this inhomogeneity on our analysis is discussed further in Sec. 4.4. We also observed that a significant number of pixels exhibited a square pattern, where the central pixel has a higher count rate than the adjacent pixels (see the inset zoom region in Fig. 2). Similarly, when we extracted two-pixel events from the datasets, we noticed an opposite pattern trend in the count map, where the central pixel has a lower count rate than the adjacent pixels. These patterns appear to be associated with

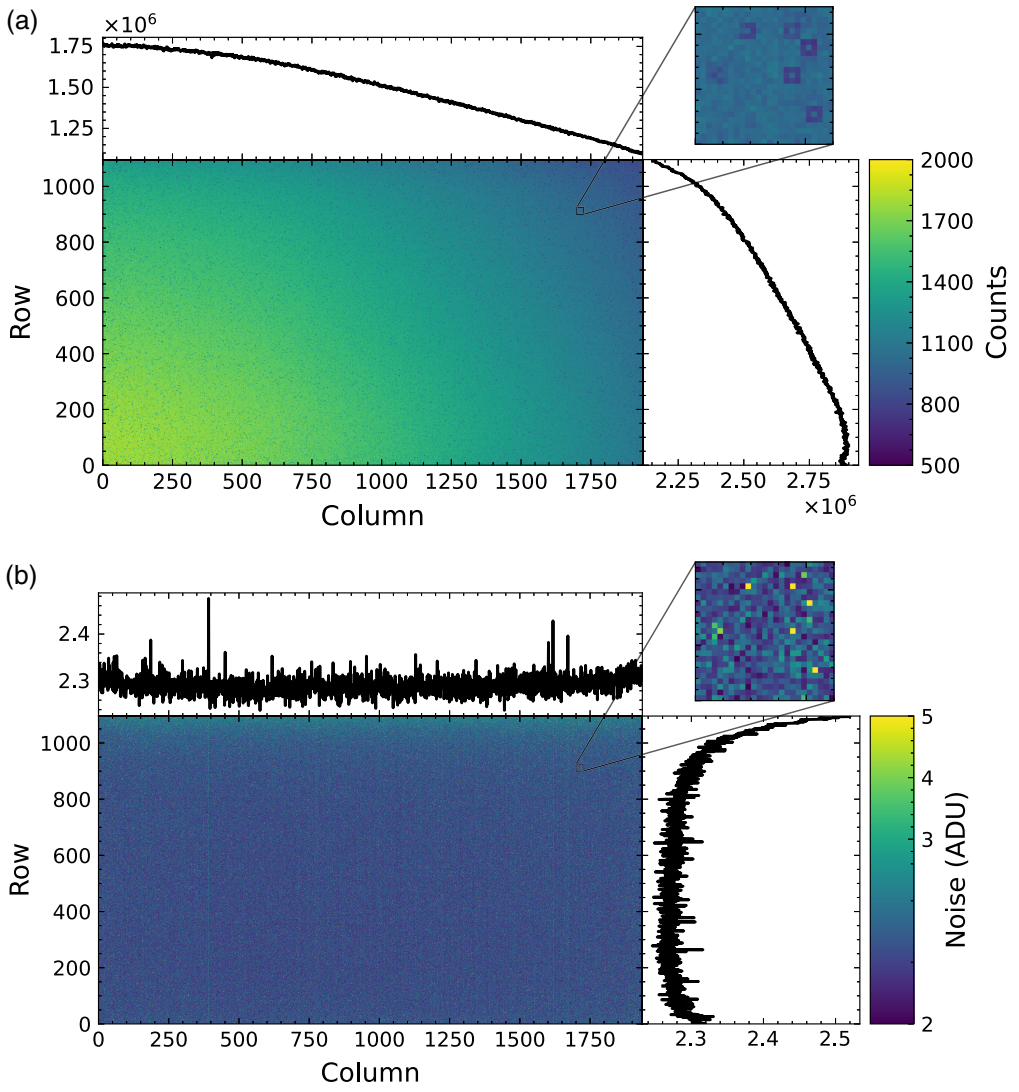

Fig. 2 (a) Count map of single-pixel events obtained after 14 days of acquisition with the ^{55}Fe source. The upper and right insets represent the sum of counts by column and row, respectively. The upper right inset shows a zoom of a small area of the sensor outlining the square patterns observed. (b) Noise map derived from 300 frames at the beginning of one of the 10-min acquisition sequences. The upper and right insets show the average noise by column and row, respectively. The upper right inset shows a zoom-in on a small region of the sensor, highlighting the pixels with higher noise than average producing the squared patterns observed on the count map.

pixels with higher noise levels, as shown in the noise map in Fig. 2(b). In this respect, pixels with higher noise levels cause the migration of single-pixel events into two-pixel events in adjacent pixels. This is a consequence of using the same split threshold for all pixels during the event extraction process. Implementing a pixel-dependent split threshold based on individual noise levels would mitigate this effect and result in a more homogeneous count map.

We ended up with one spectrum for each of the 2.1 million pixels, made up entirely of single-pixel events. Figure 3 shows an example of two spectra from two pixels in the same column (#662) but in different rows (#192 versus #242). The two main emission lines produced by the radioactive source are clearly detected at 5.90 keV (Mn-Kα) and 6.49 keV (Mn-Kβ). In addition, the Si-K escape line of Mn-Kα (4.16 keV) is marginally detected. Both spectra were calibrated in energy with the same gain, and a small energy shift between them is noticeable, contributing to the broadening of the lines when combined. We measured a spectral resolution of 122 eV at 5.9 keV using a Gaussian fit, close to the intrinsic Fano limit at this temperature (119 eV) and consistent with a 2 $e-$ rms noise device.

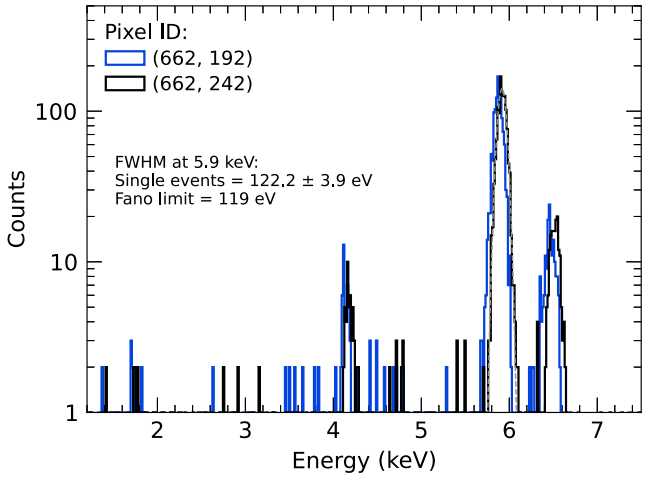

Fig. 3 ^{55}Fe spectra of single-pixel events from the same column (#662) but in different rows (#192 versus #242) of the sensor area calibrated with the same gain value. The Mn-Kα (5.90 keV) and Mn-Kβ (6.49 keV) lines produced by the ^{55}Fe radioactive source and the Si-K escape line of Mn-Kα (4.16 keV) are detected in both spectra. A small horizontal shift is visible between the two spectra. The gray dashed line shows the best-fit Gaussian model used to measure the spectral energy resolution for the pixel ID (662, 242).

4.4 Gain Measurement and Optimal Counts per Spectrum

Two different calibration methods, peak fitting and ECC, were used to determine the gain for each pixel (see Sec. 4.1). We used the enhanced version of ECC with adaptive mesh refinement[23] to discretize the parameter space and reduce the computational time.

For both methods, we assumed a linear calibration in energy, expressed as $E = \text{gain} \times PHA + \text{offset}$, where PHA is the pulse height amplitude. Because the ^{55}Fe source produces two emission lines within a limited energy range (0.5 keV), it can be challenging to constrain a small residual offset sometimes required to improve the energy calibration of some detectors. We first performed an energy calibration using the peak fitting method, considering two free parameters (gain and offset). The ratio of the offset to its error returned a median value of 1.2, suggesting that the residual offset, expected to be close to zero, cannot be well-constrained with the current data. This is supported by real-time data processing, in which the offset map subtracted from the frames prior to extracting the X-ray events is updated every 10 min. This ensures that any systematic offset drift is minimized over time and that the residual offset should tend to zero. We therefore assumed an offset of 0 for the energy calibration in the rest of our analysis.

The gain map derived by the peak fitting method considering only one free parameter (gain) is shown in Fig. 4. The gain distribution shows a normal distribution with a mean of 294 ADU/keV and a 1-sigma dispersion of 0.4%. This observed variation exceeds that reported in the literature using 5×5 binning regions (0.14%),[20] suggesting potentially significant interdevice variability or discrepancies due to the method used. The upper inset of Fig. 4 represents the average gains for each column. A difference was observed between the average gains of odd and even columns. This difference is constant along the columns ($\sim$1 ADU/keV) and larger than the standard deviation of the average column gains. This trend was not observed in the right inset of the 2D gain map (Fig. 4), where even and odd rows have consistent average gains along rows. The feature observed for the average gain columns is thought to be due to the parallelism of the readout specific to CMOS technology, where the signal from an entire row can be read out simultaneously. In this design, each column has its own second-stage signal amplifiers, correlated double sampling, and analog-to-digital converters (ADCs). In addition, these components can be distributed on either side of the sensor area to save space, with even-column components on one side and odd-column components on the other. No significant difference was observed between the gains measured by ECC and peak fitting methods, with $\widetilde{\text{gain}}_{\text{ECC}} = 293.66 \pm 1.18$ ADU/keV and $\widetilde{\text{gain}}_{\text{peak fitting}} = 293.59 \pm 1.18$ ADU/keV.

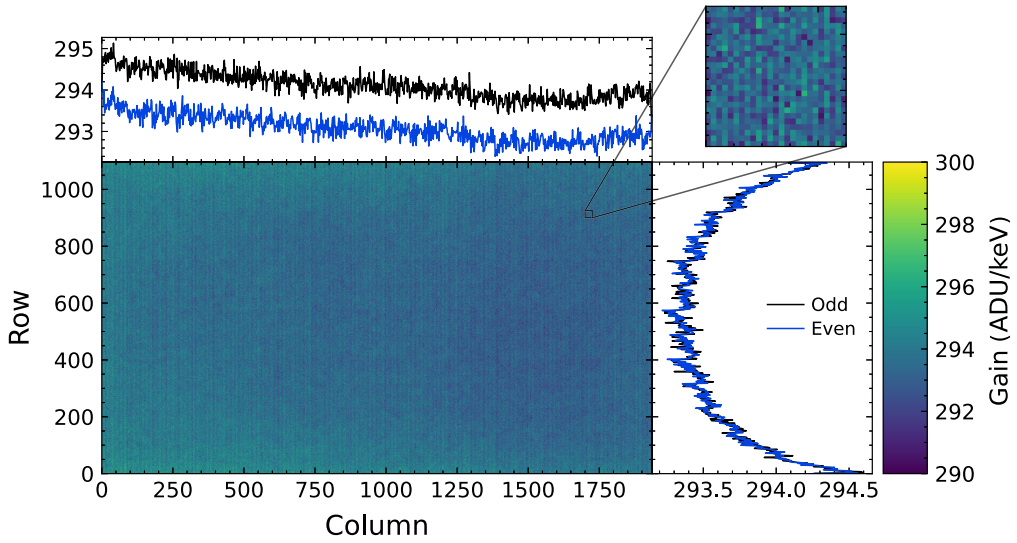

Fig. 4 Gain map derived from ^{55}Fe spectra of single-pixel events using the peak fitting method on the Mn-Kα and Mn-Kβ lines. The upper and right insets represent the average gain by column and row, respectively. Average gains for even (odd) columns and rows are indicated by blue (black) lines. The upper right inset shows a zoom of a small area of the sensor outlining the small-scale gain variation.

We investigated the performance and advantages of each method with respect to the number of single-pixel events in the spectrum (sample size). Due to the inhomogeneity observed in the count map in Fig. 2, which could bias the results, we performed this analysis by randomly selecting 10,000 pixels within the 90th to 95th percentile of the count distribution. This criterion yields an initial pixel sample of 104,737 pixels with counts between 1664 and 1720 photons. For each pixel, we generated a set of spectra with different sample sizes (10, 50, 100, 200, 500, . . . , events) by randomly selecting events from their initial distribution. For each sample size, we applied both ECC and peak fitting to the set of 10,000 spectra and measured their gains. The energy resolution of the Mn-Kα line was then determined by combining the 10,000 spectra into a single spectrum after correcting for individual gain variations. The evolution of spectral resolution as a function of sample size is shown in Fig. 5. Both methods converge to the same energy resolution when

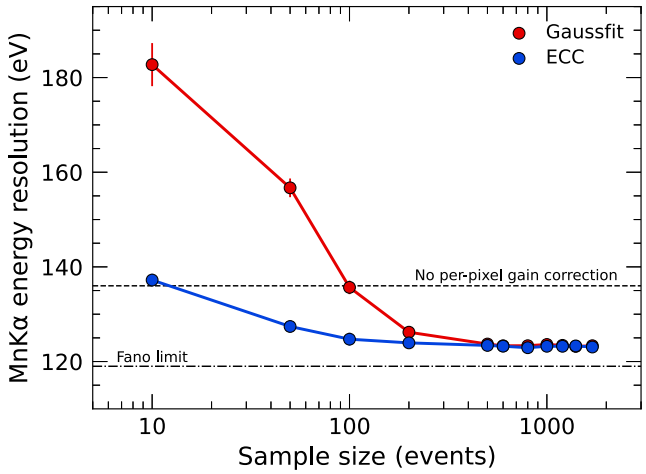

Fig. 5 Energy resolution of single-pixel events at 5.9 keV (Mn-Kα) as a function of sample size. The energy resolution is measured using a Gaussian fit on a spectrum combining 10,000 pixels from the high-count region of Fig. 2 and corrected for per-pixel gain variation using the peak fitting (red) and ECC (blue) methods. The dashed gray line represents the energy resolution assuming the same gain for all pixels. The Fano limit expected at room temperature is indicated by a dashed-dotted line.

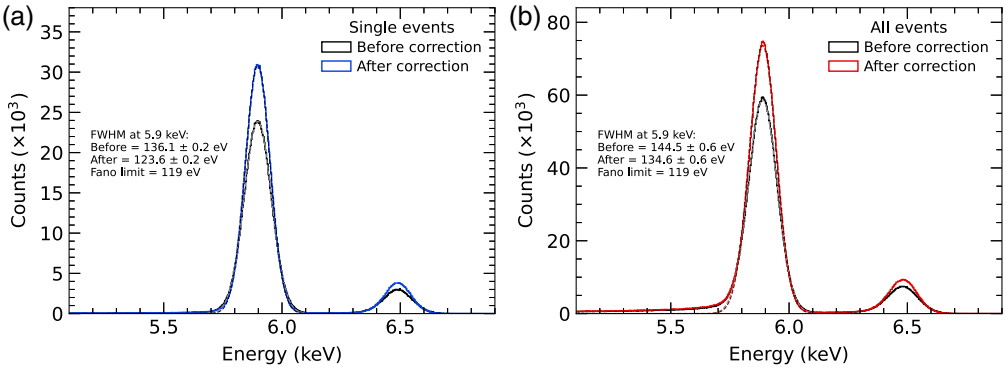

Fig. 6 Spectrum of single-pixel events (a) and all events (b) before per-pixel gain correction (in black) and after per-pixel gain correction (in blue or red). The gray, dark blue, and dark red dashed lines show the best Gaussian fit used to derive the energy resolution.

spectra are composed of more than ∼500 single-pixel events. At lower counts, the ECC method outperforms peak fitting, showing an improvement in spectral performance for statistics greater than 10 photons. In contrast, peak fitting requires a minimum of 100 photons to achieve results similar to using a single gain for all pixels. Given a gain dispersion of 0.4%, this analysis provides guidance on the optimal statistics required to accurately correct for the per-pixel gain dispersion of the sensors. As all pixels in our data set have more than 492 single-pixel events, it is unlikely that the inhomogeneous count pattern observed in the count map (Fig. 2) has affected our per-pixel gain correction.

5 X-ray Energy Resolution after Per-Pixel Gain Correction

5.1 Per-Pixel Gain Correction

Correcting the per-pixel variation of CMOS sensors is expected to improve the spectral performance of the device. To validate our gain measurement, we corrected the gain dispersion using the gain map visible in Fig. 4 on a 10-min data set, corresponding to ∼4 million photons detected. The combined spectrum of single-pixel and all events before and after the gain correction is shown in Fig. 6. As expected, the energy resolution is improved after correcting the per-pixel gain variation from 136.1 ± 0.2 eV to 123.6 ± 0.2 eV (∼12 eV) for single-pixel events and from 144.5 ± 0.6 eV to 136.1 ± 0.6 eV (∼10 eV) for all events spectra.

The improvement observed after the per-pixel gain correction confirms our ability to measure and correct the gain variation. The spectral performance of single-pixel events is approaching the theoretical limit of silicon detectors of 119 eV at room temperature (300 K) for an electron–hole pair creation energy of 3.67 eV and a Fano factor of 0.118.[25] The difference observed for single-pixel events compared with the Fano limit could be mainly attributed to the electronic noise of $\sim 2e-$ rms measured for this device. In addition, the electronic noise might increase the observed difference between single-pixel and all events to some extent by the fraction of energy loss below the split threshold, known as the charge-sharing effect, which depends on the detector geometry and multiplicities. This effect can be mitigated empirically or by Monte Carlo simulations[5] but was not corrected for in this analysis. Additional broadening of the lines compared with the Fano limit could result from the use of the same split threshold for the entire sensor area, producing the square patterns observed in Fig. 2 and the overestimation of the energy of some events.

5.2 Temperature Dependence of Gains

After a pause of 6 days, we acquired a second data set under the same configuration and operating conditions except that the camera temperature was increased from 21°C to 26°C. The objective was to investigate the temperature dependence of the gain, in particular, the per-pixel dispersion. Figure 7(a) shows the comparison of the gain distribution at the two temperatures. The gain dispersion at both temperatures was consistent at 0.4%, but the distribution showed a median shift of 0.15 ADU/keV (0.05%) when the temperature was raised by 5°C. At first order, this suggests that all pixel gains are affected in a similar way as the temperature changes and that

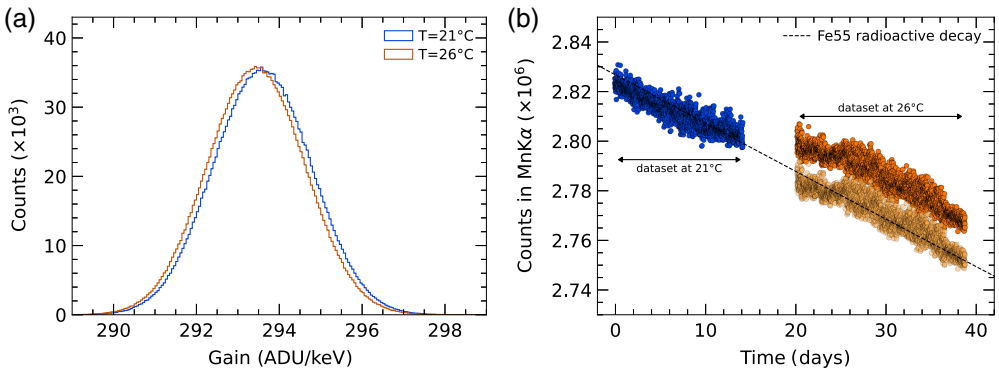

Fig. 7 (a) Histogram of the 2.1 million gains at 21°C (blue) and 26°C (orange). (b) Total number of counts per 10-min file from the Mn-Kα line ($5.7 < E < 6.1$ keV) as a function of time at 21°C (blue) and 26°C (orange). The dashed black line represents the expected radioactive decay rate of ^{55}Fe during the observation period. The lighter orange circles indicate count rates at 26°C, reduced by a constant offset of 0.5% to obtain a ^{55}Fe decay rate consistent with the one measured on the 21°C data set. The exact cause for this offset remains to be explored in future work.

the gain dispersion remains constant within the temperature variations observed during data acquisition ($\lesssim$0.2°C). In a broader context, measuring the per-pixel gain dispersion at one temperature may offer the possibility of mitigating the gain dispersion at another temperature, at least within a certain temperature range. Additional data sets over a broader temperature range are needed to confirm the temperature dependence of the gains.

5.3 Device Stability over Time

Our long acquisition data sets allow us to measure the stability of the device over several days at a high count rate (~7000 counts per second). In Fig. 7(b), the total number of counts per 10 min file from the Mn-Kα ($5.7 < E < 6.1$ keV) is shown for both temperatures. Hot pixels have been removed from each file, and the gain temperature dependence observed in Fig. 7(a) has been corrected. We observed that at both temperatures the count rate in the Mn-Kα line decreases progressively with time. The measured decay is consistent with the expected radioactive decay rate of ^{55}Fe (half-life decay of 2.737 years) over this period. However, we noticed an additional constant offset of ~0.5% in the counts to the expected trend at 26°C. By removing this offset, we can obtain a decay consistent with the data set acquired at 21°C. The exact reasons for this offset will be the subject of future work.

All pixels with an abnormal count rate (more than 10 counts per 10 min) were considered as hot pixels. The number of hot pixels was very stable over time for both temperatures, with a median number of hot pixels of 39 ± 6 at 21°C and 44 ± 6 at 26°C. At 26°C, we also saved the offset and noise map every 10 min to track their evolution over time. We found that the noise was very stable, with an equivalent electronic noise of $2.10^{+0.05}_{-0.01}$ $e-$ rms. The offset level was configured to a value of 200 ADU, and we measured a value of $199.76^{+0.60}_{-0.63}$ ADU, corresponding to a fluctuation of ~1 $e-$ over 16 days. Our measurements demonstrated excellent stability in terms of readout noise, hot pixels, and dark current level of the camera over more than 30 days of data acquisition.

6 Conclusion

We investigated the per-pixel gain calibration of the Sony IMX290 CMOS sensor composed of more than 2.1 million pixels. We collected X-ray photons from a ^{55}Fe radioactive source under stable conditions over a period of two weeks at room temperature (21°C), to obtain more than 500 single-pixel events per pixel and generate a single-event spectrum per pixel. We used two energy calibration methods (peak fitting and ECC) to measure the gain of all pixels and investigated the possible advantages of each method. ECC outperformed peak fitting in the case of low statistics and offers a promising prospect for per-pixel gain correction of CMOS sensors. Our gain measurements showed good overall gain homogeneity and a gain dispersion of 0.4% for the entire sensor area. However, a constant difference along the columns of ~1 ADU/eV was

noted between the average gains of the odd and even columns. Once corrected for per-pixel gain dispersion, we confirmed that the spectral performance was improved by $\gtrsim$10 eV at 5.9 keV. The spectral performance of single-pixel events was found close to the Fano limit at room temperature as expected for a $2e-$ rms readout noise device and demonstrated the impressive spectral performance of the sensor relative to its low cost. We repeated the measurement at a temperature $+5$°C higher (26°C) and observed a small shift (0.05%) in the central value of the gain distribution, whereas the gain dispersion remained stable at 0.4%. Furthermore, both data sets confirmed the excellent stability of the device with regard to noise, hot pixels, and offsets over 30 days of acquisition under a count rate of more than 7000 counts per second. Further work on the Sony IMX290 CMOS sensor is needed to confirm its potential use in X-ray astronomy, such as measuring its X-ray quantum efficiency.

Disclosures

The authors declare no relevant financial interests or potential conflicts of interest related to this paper.

Code and Data Availability

The data and codes utilized in this study are not publicly available and are the property of the Massachusetts Institute of Technology. They can be requested from the authors at bschn@mit.edu. The energy calibration via correlation (ECC) code is the property of the Commissariat à l'Energie Atomique et aux Energies Alternatives (CEA).

Acknowledgments

The authors acknowledge the MIT SuperCloud and Lincoln Laboratory Supercomputing Center for providing (HPC, database, consultation) resources that have contributed to the research results reported within this paper. They also acknowledge support from the MIT Kavli Institute's Research Investment Fund.

References

1. L. Strüder et al., "The European Photon Imaging Camera on XMM-Newton: the pn-CCD camera," *Astron. Astrophys.* **365**, L18–L26 (2001).
2. G. P. Garmire et al., "Advanced CCD imaging spectrometer (ACIS) instrument on the Chandra X-ray Observatory," *Proc. SPIE* **4851**, 28–44 (2003).
3. K. Koyama et al., "X-ray imaging spectrometer (XIS) on board Suzaku," *Publ. Astron. Soc. Jpn.* **59**, S23–S33 (2007).
4. P. Predehl et al., "The eROSITA X-ray telescope on SRG," *Astron. Astrophys.* **647**, A1 (2021).
5. B. Schneider et al., "Spectral performance of the Microchannel X-ray Telescope on board the SVOM mission," *Exp. Astron.* **56**, 77–97 (2023).
6. M. Bautz et al., "Progress toward fast, low-noise, low-power CCDs for Lynx and other high-energy astrophysics missions," *Proc. SPIE* **11444**, 1144494 (2020).
7. B. J. LaMarr et al., "Measurement and simulation of charge diffusion in a small-pixel charge-coupled device," *J. Astron. Telesc. Instrum. Syst.* **8**(1), 016004 (2022).
8. E. D. Miller et al., "Understanding the effects of charge diffusion in next-generation soft X-ray imagers," *Proc. SPIE* **12181**, 121816R (2022).
9. E. D. Miller et al., "The high-speed X-ray camera on AXIS," *Proc. SPIE* **12678**, 1267816 (2023).
10. W. Yuan et al., "The Einstein probe mission," in *Handbook of X-ray and Gamma-ray Astrophysics*, C. Bambi and A. Sangangelo, Eds., Vol. **86**, Springer, Singapore (2022).
11. C. Zhang et al., "First wide field-of-view X-ray observations by a lobster-eye focusing telescope in orbit," *Astrophys. J. Lett.* **941**, L2 (2022).
12. Y. Liu et al., "Soft X-ray prompt emission from a high-redshift gamma-ray burst EP240315a," arXiv:2404.16425 (2024).
13. A. J. Levan et al., "The fast X-ray transient EP240315a: a z $\sim$ 5 gamma-ray burst in a Lyman continuum leaking galaxy," arXiv:2404.16350 (2024).
14. K. D. Stefanov and A. D. Holland, "CMOS active pixel sensors," in *Handbook of X-ray and Gamma-ray Astrophysics*, C. Bambi and A. Sangangelo, Eds., Vol. **14**, Springer, Singapore (2022).
15. Q. Wu et al., "X-ray performance of a customized large-format scientific CMOS detector," *Publ. Astron. Soc. Pac.* **134**, 035006 (2022).

16. C. Townsend-Rose et al., "Electro-optical characterization of a CMOS image sensor optimized for soft x-ray astronomy," *J. Astron. Telesc. Instrum. Syst.* **9**(4), 046001 (2023).
17. W. X. Wang et al., "Characterization of a BSI sCMOS for soft X-ray imaging spectroscopy," *J. Instrum.* **14**, P02025 (2019).
18. N. Narukage et al., "High-speed back-illuminated CMOS sensor for photon-counting-type imaging-spectroscopy in the soft X-ray range," *Nucl. Instrum. Methods Phys. Res. A* **950**, 162974 (2020).
19. Y. Hsiao et al., "X-ray performance of a small pixel size sCMOS sensor and the effect of depletion depth," *J. Instrum.* **17**, P12006 (2022).
20. S. Tammes et al., "Soft x-ray detection for small satellites with a commercial CMOS sensor at room temperature," *J. Astron. Telesc. Instrum. Syst.* **6**(4), 046004 (2020).
21. T. Roth et al., "Characterization of gamma-ray-induced radiation effects on a commercial CMOS sensor for x-ray small satellites," *J. Astron. Telesc. Instrum. Syst.* **8**(2), 026001 (2022).
22. D. Maier and O. Limousin, "Energy calibration via correlation," *Nucl. Instrum. Methods Phys. Res. A* **812**, 43–49 (2016).
23. D. Maier, O. Limousin, and G. Daniel, "Energy calibration via correlation using an adaptive mesh refinement," in *Eur. Phys. J. Web of Conf.*, Vol. 225, p. 01003 (2020).
24. A. Reuther et al., "Interactive supercomputing on 40,000 cores for machine learning and data analysis," in *IEEE High Perform. Extreme Comput. Conf. (HPEC)*, pp. 1–6 (2018).
25. B. G. Lowe and R. A. Sareen, "A measurement of the electron hole pair creation energy and the Fano factor in silicon for 5.9 keV X-rays and their temperature dependence in the range 80 270 K," *Nucl. Instrum. Methods Phys. Res. A* **576**, 367–370 (2007).

Benjamin Schneider is a postdoctoral researcher at the MIT Kavli Institute, working at the interface of high-energy astrophysics and instrumentation. His previous work includes energy calibration and characterization of the Microchannel X-ray Telescope (MXT) onboard the SVOM mission. He worked on the morphology of gamma-ray burst (GRB) host galaxies using Hubble Space Telescope (HST) images and regularly performs optical follow-up observations of GRBs using ground-based facilities such as the Very Large Telescope.

Catherine E. Grant received her bachelor's degree in astronomy and astrophysics from Harvard University in 1993 and her PhD in astronomy and astrophysics from Penn State University in 1999. She is currently a research scientist at the MIT Kavli Institute for Astrophysics and Space Research. Her work includes characterizing radiation damage in the Chandra ACIS CCDs, developing software techniques for mitigating charge transfer inefficiency and flight software algorithms to allow ACIS to act as its own radiation monitor, and efforts to reduce and understand the particle background in future X-ray missions using in situ particle data and Geant4 simulations.

Jill Juneau, an electrical engineer at MIT's Kavli Institute (2023), specializes in detector instrumentation and characterization, collaborating across projects, including a sounding rocket X-ray detector telescope (REDSoX), and a land-based near-infrared detector telescope (WINTER). Previously, she was employed in telemetry systems for NASA's balloon program and managed an instrumentation group at LSU's Physics Department with the design for T2K's Super-FGD neutrino detector. Her graduate research at Rice University (MS EE 2020) focused on miniaturized microscopes for neural imaging.

Olivier Limousin is a research director at CEA/Irfu in the field of instrumentation for space sciences. He is a recognized international expert in semiconductor-based X and gamma-ray imaging spectrometers, associated CMOS electronics, and 3D hybridization technologies. He was involved in many space-science projects such as Integral and Solar Orbiter (ESA), ASTRO-H (JAXA), CINEMA Trio (UCB/SSL and NSF), SVOM/ECLAIRs (CNES/CAS), and PADRE (UCB/SSL, NASA) and is contributing to the industrial deployment of CALISTE detectors technology into nuclear applications.

Eric D. Miller received his BA degree in physics from Oberlin College in 1996 and his MS and PhD degrees in astronomy and astrophysics from the University of Michigan in 1998 and 2003, respectively. He is a research scientist at the MIT Kavli Institute for Astrophysics and Space Research. He leads the XRISM In-Flight Calibration Planning Team, develops X-ray imaging detectors for future missions, and studies galaxy clusters and the diffuse intergalactic medium.

Biographies of the other authors are not available.